# nBn mid-wavelength infrared photodetectors based on bulk InGaAsSb absorber

PENG CAO,[1,2] JIAQI WEI,[1,3] MATTHEW BENTLEY,[4] NICHOLAS DAVISON,[4] YIDAN HU,[4] MINGHUI YOU,[5] HONGLING PENG,[1,2] TIANCAI WANG,[6] QIANDONG ZHUANG,[4] AND WANHUA ZHENG[1,2,3,6 *]

[1] *Laboratory of Solid State Optoelectronics Information Technology, Institute of Semiconductors, CAS, Beijing 100083, China*
[2] *State Key Laboratory on Integrated Optoelectronics, Institute of Semiconductors, CAS, Beijing 100083, China*
[3] *College of Electronic and Communication Engineering, University of Chinese Academy of Sciences, Beijing 101408, China*
[4] *Physics Department, Lancaster University, Lancaster LA1 4YB, UK*
[5] *College of Engineering and Technology, Jilin Agricultural University, 2888 Xincheng Street, Changchun 130118, China*
[6] *Hangzhou Institute for Advanced Study, University of Chinese Academy of Sciences, Hangzhou 310024, China*
**whzheng@semi.ac.cn*

**Abstract:** In this paper, we demonstrate an nBn mid-wavelength infrared (MWIR) photodetector with a 100% cutoff wavelength over 4.0 μm based on high-In composition InGaAsSb absorber on GaSb substrate. A thin AlGaAsSb layer is exploited as the barrier layer to suppress the generation-recombination (G-R) current. Both structural and optical properties of the grown InGaAsSb epilayer are investigated by high-resolution X-ray diffraction (HRXRD) and photoluminescence (PL) measurement. Low dark current density down to $9.9\times10^{-5}$ A/cm$^2$ and $6.5\times10^{-2}$ A/cm$^2$ are obtained at -500 mV under 77 K and 300 K, respectively. Moreover, respective peak responsivity of 0.64 A/W and 0.10 A/W at 2.67 μm are achieved at -500 mV under 77 K and 160 K. These correspond to a peak specific detectivity of $1.06\times10^{11}$ cm·Hz$^{1/2}$/W and $4.23\times10^{9}$ cm·Hz$^{1/2}$/W , respectively.



## 1. Introduction

Detection of mid-wavelength infrared (MWIR), from 3 μm to 5 μm, has attracted great attention due to a wide range of applications in this spectrum, including gas sensing, imaging systems especially for observing hot objects and identification surveillance[1-4]. Photodetectors based on various material systems working towards mid-wavelength have been investigated. HgCdTe (MCT) based MWIR photodetectors present high flexibility due to highly tunable band gap [5, 6] but suffer low crystalline quality for large arrays and high cost associated with complicated fabrication process[7]. InAs/GaSb and InAs/GaSb/AlSb based Type-II superlattice (T2SL) structures [8, 9] are alternative proper candidates for MWIR detection attributed to the long Auger lifetime [10] and high carrier effective mass [11]. However, T2SL based MWIR photodetectors still presents high dark current density attributed to the low Shockley-Read-Hall (SRH) lifetime [12] and low quantum efficiency.

In this paper, we utilize a quaternary compound InGaAsSb material with a high In composition of 0.9 to fabricate an nBn type MWIR photodetectors on GaSb substrate. Structural property, surface morphology and optical properties of grown InGaAsSb epilayer on GaSb are investigated and analyzed. Dark current performance as well as the optical response and calculated specific detectivity are presented and discussed. This work provides instruction

for further optimization of MWIR photodetectors based on bulk absorber material and design for MWIR avalanche photodiodes.

## 2. Experimental methods

### *2.1 Material growth and device fabrication*

The photodetector structure is grown by molecular beam epitaxy at temperature of 480 ℃. The schematic diagram of the cross section of the whole device is shown in Figure. 1(a). After the desorption of native oxides of the substrate, the growth process is started with the deposition of 100 nm-thick GaSb buffer followed by a heavily n-doped InGaAsSb layer as the bottom contact layer. Next, a 2 μm thick unintentionally doped InGaAsSb absorption layer was grown. After that, an 80 nm thick AlGaAsSb barrier layer is grown in a Sb-rich atmosphere. Pre-calibrated optimal beam equivalent pressure (BEP) ratio of five is set throughout the whole structure while the BEP for Ga is set to be $3\times10^{-7}$ mbar, which gives rise to a growth rate of 0.68 μm/h for GaSb throughout the structure with corresponding growth rate for InAs and AlSb to match the designed compositions in InGaAsSb and AlGaAsSb. Finally, a 160 nm thick InGaAsSb layer is deposited as the top contact layer. The In compositions of bottom contact, absorption layer and top contact InGaAsSb layer are designed to be 0.9 and the corresponding As composition is designed to be 0.81 for lattice matched to the GaSb substrate. The fabrication process of mesa type photodetector device is based on standard lithography. Figure .1 (b) and (c) show the microscope image of the single pixel and SEM image of the Inductively coupled plasma (ICP) etched mesa surface, respectively. The operating temperature for ICP process is 180℃ and the gas etchants consisting of $CH_4$, $Cl_2$ and Ar are utilized to assure the smooth sidewall.

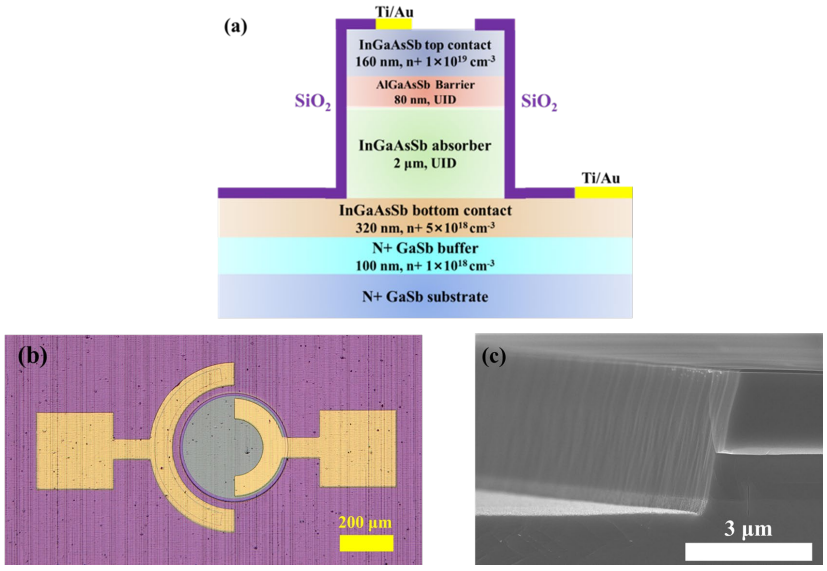


**Fig. 1.** (a) Cross section schematic diagram and (b) microscope image of nBn MWIR InGaAsSb photodetector. (c) SEM image of ICP etched mesa surface of the MWIR device.

### *2.2 Characterization of material quality*

High resolution X-ray diffraction (HRXRD) scan of the nBn MWIR photodetector is shown in Figure. 2(a). A slight separation between the peak of high In composition epilayer and the GaSb substrate peak indicates that a near lattice matched condition is obtained. The extracted In composition and As composition of InGaAsSb layer is 0.9 and 0.81 which is consistent with

the designed value. The peak of the AlGaAsSb barrier overlap perfectly with the GaSb substrate peak with an extracted Al composition of 0.34. The XRD results show that a high quality nBn InGaAsSb structure is achieved.

Typical AFM image with 20×20 $\mu m^2$ scan area is shown in Figure. 2(b). Root-mean-square (RMS) roughness extracted from AFM images indicates the quality of surface morphology after the growth of epitaxy layer which is lattice mismatched to the substrate. The RMS roughness of the high In composition InGaAsSb surface is 0.563 nm demonstrating a smooth surface is obtained and there are few dislocations formed in the InGaAsSb epilayer during the growth process.

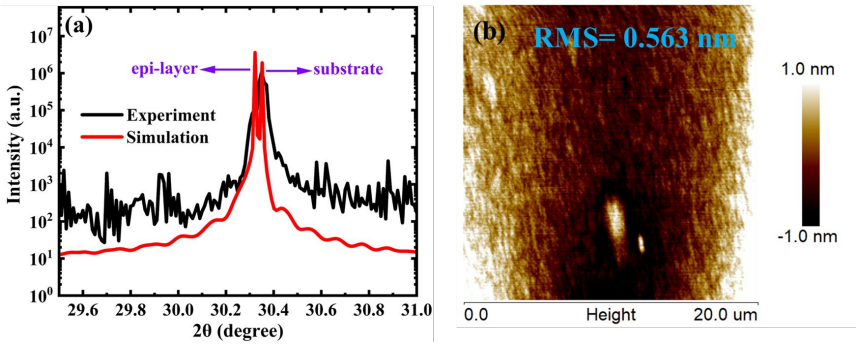


**Fig. 2.** (a) HRXRD scan of InGaAsSb epilayer (b) AFM image of InGaAsSb surface grown on GaSb substrate.

The photoluminescence (PL) spectrum measurement is set up with a 650 nm excitation laser and related analyses for the nBn MWIR InGaAsSb photodetector are presented in Figure. 3 (a) to (e). Figure. 3(a) presents the PL spectrum under varying excitation power from 10 mW to 250 mW at 8 K. The spectrum shows a multi-peak profile and the PL intensity increases as the incident power increases and the peak wavelength remains nearly the same at 3.81 μm. Multiple Gaussian peak fit (MGPF) method is taken to further investigate the asymmetric lineshape of the power dependent PL spectrum, as shown in Figure. 3(c). The MGPF results mark out the fitted Gaussian peak with peak wavelength and the overall simulation spectrum. It is worth noting that under low incident powers, i.e. at 10 mW, the PL spectrums are fitted with two Gaussian peaks: peak 1 with a short wavelength at 3.82 μm and peak 2 with a long wavelength at 3.96 μm, which slightly blue-shifted to 3.81 μm and red-shifted to 3.98 μm respectively at a higher power of 20 mW. The peak 1 is associated with the band-to-band transition and the peak 2 is believed to be related to the defect states. The defect states show zero momentum and as a result, the electrons with zero momentum in the low doped absorption layer present a higher probability to recombine with those defect states, hence the longer emission wavelength is observed [13, 14]. When the incident power surpasses 20 mW, a peak 3 is presented with a shortest wavelength of 3.72 μm, This peak shows a slight blueshift with increased excitation power as shown in Figure.3(d), eg. 3.70 μm, 3.68 μm and 3.67 μm for the incident power of 40 mW, 80 mW, 150 mW and 250 mW, respectively. In addition, as shown in Figure. 3(c), the intensity of peak 3 increases slightly with increasing incident power. Based on these behaviors, we suggest peak 3 is due to the split of heavy hole and light hole bands which increase the transition energy for electrons. Considering the realistic application of photodetectors, a typical incident power magnitude of tens of watt is preferrable so that the PL spectrum of the grown nBn MWIR under low incident power illumination satisfies our requirements. It is worth noting that no emission that is associated with localized stated formed by content nonuniformity is observed in our samples, together with the narrow peak linewidth of X-ray diffraction we confirm the highly uniform crystalline quality of the alloy.

Temperature dependent PL spectrum from 8 K to 290 K and the related analyses are shown in Figure. 3(b) and (d). By increasing temperature, a red shift is observed of the peak of the PL spectrum due to the shrinkage of the band gap energy. Moreover, the PL intensity drops dramatically indicating the increasing numbers of the nonradiative recombination centers. Figure. 3(e) presents the Arrhenius plot of integrated PL intensity over the temperature range from 8 K to 290 K according equation (1) below [15]:

$$I(T) = \frac{I_0}{1 + A\exp(-\frac{E_{a1}}{kT}) + B\exp(-\frac{E_{a2}}{kT})} \quad \text{.....(1)}$$

where $I(T)$ is the temperature-dependent integrated PL intensity, $I_0$ is the integrated PL intensity at low temperatures, $k$ is the Boltzmann's constant, $A$ and $B$ are rate constants referring to the ratios of nonradiative to radiative recombination probabilities for the two non-radiative process. $E_{a1}$ and $E_{a2}$ are the activation energies for two temperature ranges, respectively.

The integrated PL intensity present a significant drop after the temperature surpass 40 K which is attributed to the thermal quenching by the phonon-assisted non-radiative recombination process [16]. As a result, two activation energies $E_{a1}$ and $E_{a2}$ are extracted corresponding to two temperature channels: 8 K to 40 K and 40 K to 290 K. $E_{a1}$ for low temperature channel is related to the interfacial roughness [17] and the value of $E_{a1}$ is 11.8 eV. While $E_{a2}$ for high temperature channel is correlated with non-radiative process due to the misfit dislocations [18, 19]. A higher $E_{a2}$ gives rises to a lower density of activated non-radiative recombination centers, leading to a higher quantum efficiency. The extracted $E_{a2}$ value is 49.6 meV as shown in Figure.3(e).

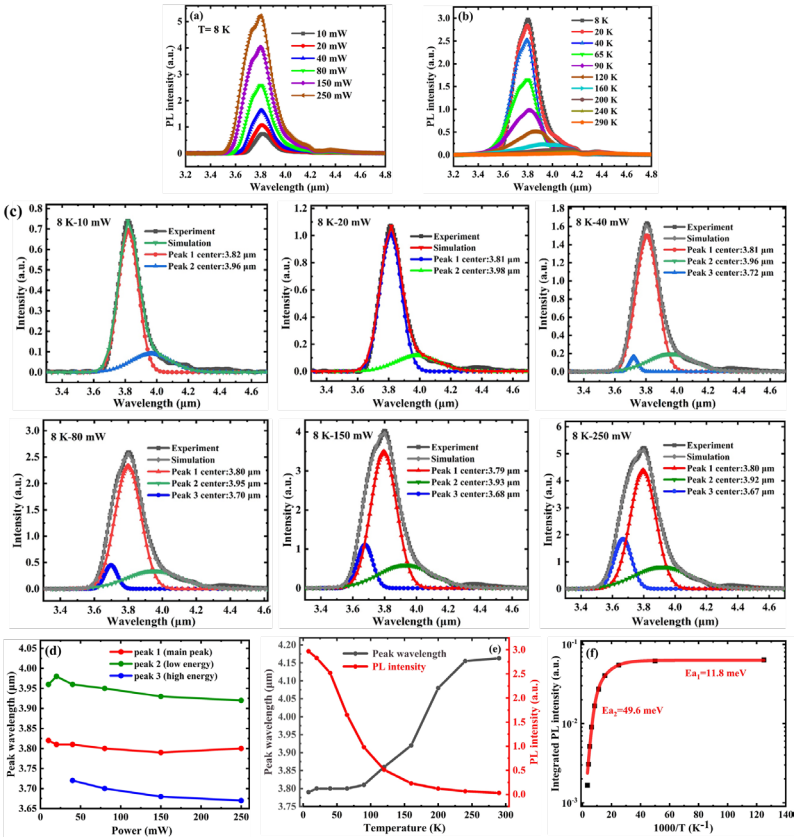

**Fig. 3.** (a) Power and (b) temperature dependent PL spectrum of nBn MWIR InGaAsSb photodetector. (c) Multiple Gaussian peak fit of power dependent PL spectrum at 8 K. (d) PL peak energy shift of fitted peaks in Fig. 3(c) vary as incident power (e) PL peak shift and intensity vary as temperature. (f) Arrhenius plot of integrated PL intensity of nBn MWIR InGaAsSb photodetector over the temperature range from 8 K to 290 K.

## 3. Electrical and optical performance of nBn MWIR InGaAsSb photodetectors

### *3.1 Band diagram simulation of nBn MWIR InGaAsSb photodetector*

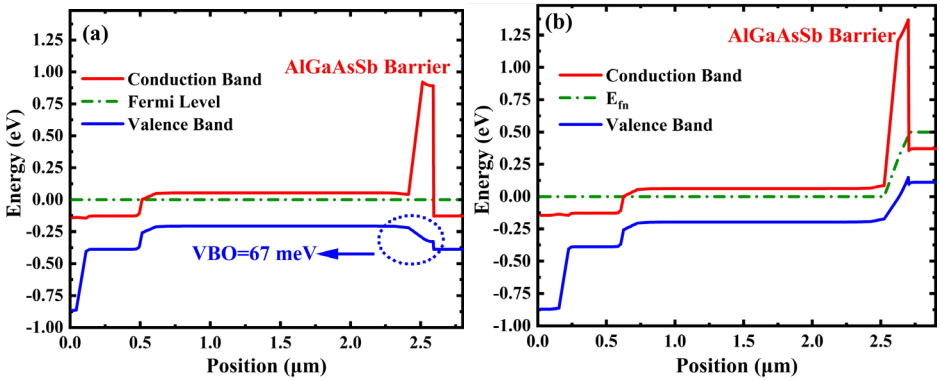


**Fig. 4.** Simulation results of band diagram of nBn MWIR InGaAsSb photodetector under (a) equilibrium condition (b) reverse bias of -500 mV.

Band diagrams of these nBn MWIR InGaAsSb photodetectors under equilibrium state and 500 mV reverse biased state are simulated by SILVACO TCAD software as shown in Figure.4(a) and (b), respectively. Under zero bias condition, the insert of AlGaAsSb electron barrier provide a high conduction band offset (CBO) near 1 eV while a valence band offset (VBO) down to 67 meV is observed. The photogenerated electrons flow in the absorption region is impeded by this barrier layer and directly move towards the bottom contact. After a reverse bias of 500 mV is applied, it is worth noting that the band bending of the Fermi energy level completely occurs in the wide band gap AlGaAsSb barrier layer, indicating the depletion region are not extending into the narrow band gap InGaAsSb absorption layer. As a result, the generation-recombination (G-R) dark current is suppressed, which is consistent with the principle of the nBn structure design [20].

### *3.2 Dark current characteristic of nBn MWIR InGaAsSb photodetector*

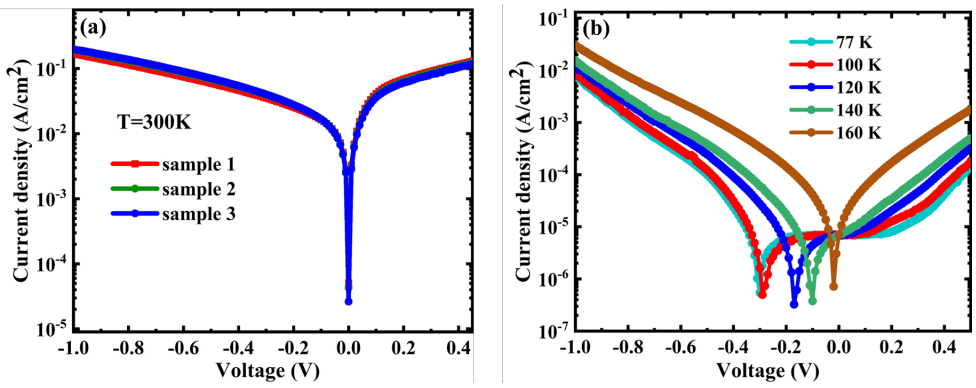


**Fig. 5.** (a) Room temperature dark current characteristic of nBn MWIR InGaAsSb photodetector. (b) Temperature dependent dark current characteristic of nBn MWIR InGaAsSb photodetector from 77 K to 160 K.

Figure. 5(a) shows the measured dark current-voltage characteristics of the nBn type MWIR InGaAsSb photodetectors at room temperature for three different samples. Under reverse bias of 500 mV, the average dark current density of $6.5\times10^{-2}$ A/cm$^2$ is obtained. In Figure. 5(b), dark current varying with temperature from 77 K to 160 K is measured and a low dark current density of $9.9\times10^{-5}$ A/cm$^2$ is achieved. The lowest point of the dark current curves shift towards the larger reverse bias as the temperature decreases from 160 K to 77 K is attributed to the photovoltaic effect induced by the thermal effect of the measurement setup.

### *3.3 Optical response of nBn MWIR InGaAsSb photodetector*

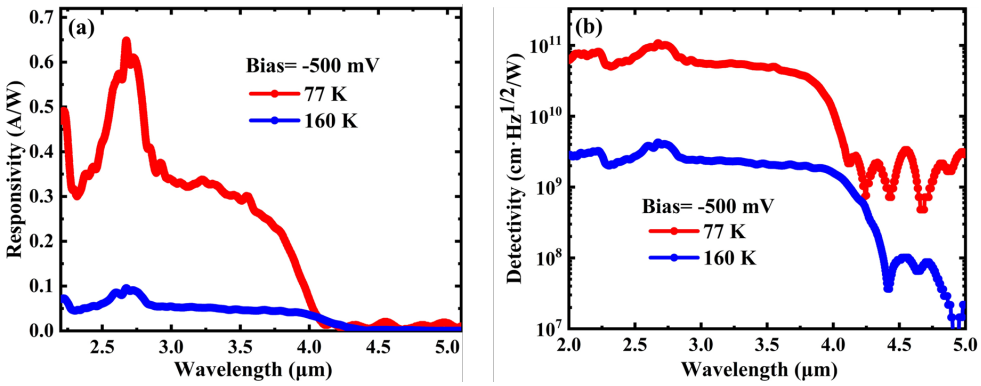


**Fig. 6.** (a) Responsivity and (b) specific detectivity of nBn MWIR InGaAsSb photodetector under 77 K and 160 K at -500 mV.

Figure. 6(a) presents the responsivity of the nBn MWIR InGaAsSb photodetector at reverse bias of 500 mV at 77 K and 160 K, respectively. The 100 % cutoff wavelength of the device are both above 4.0 μm. A peak responsivity of 0.64 A/W and 0.10 A/W are obtained at 2.67 μm at 77 K and 160 K, respectively. The high responsivity at lower temperature is due to the longer carrier lifetime of the photo-generated carriers in the InGaAsSb absorber. As the temperature goes down, the Shockley-Read-Hall (SRH) recombination and Auger recombination process are significantly suppressed, leading to an increase of the carrier lifetime. The calculated detectivity dominated by shot noise is shown in Figure. 6(b). At 77 K, the detectivity of the nBn MWIR InGaAsSb photodetectors is $1.06\times10^{11}$ cm·Hz$^{1/2}$/W and significantly drops to $4.23\times10^{9}$ cm·Hz$^{1/2}$/W at 160 K due to the increasing dark current when the temperature increases.

## 4. Conclusion

In this paper, we demonstrate nBn MWIR InGaAsSb based photodetectors. Structural properties are characterized by HRXRD scan and AFM test, and optical property is carried out by PL measurement. Moreover, the optoelectronic performance of the fabricated nBn MWIR photodetectors are presented. At 300 K, the average dark current density of the nBn MWIR InGaAsSb photodetectors is $6.5\times10^{-2}$ A/cm$^2$ at a reverse bias of 500 mV. Temperature dependent dark current characteristic from 77 K to 160 K is presented and a low dark current down to $9.9\times10^{-5}$ A/cm$^2$ is achieved. Spectral response and calculated detectivity are obtained under 77 K and 160 K. The peak responsivities are 0.64 A/W and 0.10 A/W at 2.67 μm for 77 K and 160 K, respectively, while the peak detectivities at 77 K and 160 K are $1.06\times10^{11}$ cm·Hz$^{1/2}$/W and $4.23\times10^{9}$ cm·Hz$^{1/2}$/W, respectively. This work provides further

instruction for design of high performance MWIR photodetector based on bulk absorber materials.


## Funding

This work is supported by National Science and Technology Major Project (2018YFE0200900)


## Disclosure

The authors declare no conflicts of interest.

## Data Availability

Data underlying the results presented in this paper are not publicly available at this time but may be obtained from the authors upon reasonable request.

## References


1. A. Lambrecht and K. Schmitt, "Mid-infrared gas-sensing systems and applications," in *Mid-infrared Optoelectronics* (2020), pp. 661-715.
2. H. Lin, et al., "High-Performance Room-Temperature Extended-Wavelength InAs-Based Middle-Wavelength Infrared Photodetector," physica status solidi (a) **218**(2021).
3. A. O. Karali, et al., "Multiscale contrast direction adaptive image fusion technique for MWIR-LWIR image pairs and LWIR multifocus infrared images," Applied Optics **54**(2015).
4. Z. Wu and X. Wang, "Non-uniformity correction for medium wave infrared focal plane array-based compressive imaging," Opt Express **28**, 8541-8559 (2020).
5. A. M. Itsuno, et al., "Mid-wave infrared HgCdTe nBn photodetector," Applied Physics Letters **100**(2012).
6. M. Kopytko and A. Rogalski, "HgCdTe barrier infrared detectors," Progress in Quantum Electronics **47**, 1-18 (2016).
7. A. Rogalski, "Recent progress in infrared detector technologies," Infrared Physics & Technology **54**, 136-154 (2011).
8. A. Haddadi, et al., "Bias-selectable dual-band mid-/long-wavelength infrared photodetectors based on InAs/InAs1−xSbx type-II superlattices," Applied Physics Letters **106**(2015).
9. A. M. Hoang, et al., "Demonstration of high performance bias-selectable dual-band short-/mid-wavelength infrared photodetectors based on type-II InAs/GaSb/AlSb superlattices," Applied Physics Letters **102**(2013).
10. G. G. Zegrya and A. D. Andreev, "Mechanism of suppression of Auger recombination processes in type-II heterostructures," Applied Physics Letters **67**, 2681-2683 (1995).
11. A. Dehzangi, et al., "nBn extended short-wavelength infrared focal plane array," Opt Lett **43**, 591-594 (2018).
12. X. Zhang, et al., "High-performance midwavelength infrared detectors based on InAsSb nBn design*," Chinese Physics B **29**(2020).
13. K. Grodecki, et al., "Heavily Si-doped InAs photoluminescence measurements," Materials Science-Poland **35**(2017).
14. M. Sonner, et al., "Carrier concentration dependent photoluminescence properties of Si-doped InAs nanowires," Applied Physics Letters **112**(2018).
15. B. Smiri, et al., "Optical and structural properties of In-rich InxGa1− xAs epitaxial layers on (1 0 0) InP for SWIR detectors," Materials Science and Engineering: B **262**, 114769 (2020).
16. H. Mehdi, et al., "Monolithically integrated InGaAs/AlGaAs multiple quantum well photodetectors on 300 mm Si wafers," AIP Advances **11**(2021).
17. X. Li, et al., "Enhanced properties of extended wavelength InGaAs on compositionally undulating step-graded InAsP buffers grown by molecular beam epitaxy," Crystals **11**, 1590 (2021).
18. G. Yi, et al., "Structural and photoluminescence properties for highly strain-compensated InGaAs/InAlAs superlattice," Chinese Physics Letters **26**, 077808 (2009).
19. X. Chen, et al., "Analysis of dark currents and deep level traps in InP-and GaAs-based In0. 83Ga0. 17As photodetectors," Journal of Crystal Growth **477**, 82-85 (2017).
20. S. Maimon and G. Wicks, "nBn detector, an infrared detector with reduced dark current and higher operating temperature," Applied Physics Letters **89**(2006).